



Selective Aster inhibitors distinguish vesicular and nonvesicular sterol transport mechanisms

Xu Xiao^{a,b,1}, Youngjae Kim^{c,1}, Beatriz Romartinez-Alonso^{d,1}, Kristupas Sirvydis^d, Daniel S. Ory^e, John W. R. Schwabe^d, Michael E. Jung^c, and Peter Tontonoz^{a,b,2}

^aDepartment of Pathology and Laboratory Medicine, University of California, Los Angeles, CA 90095; ^bDepartment of Biological Chemistry, University of California, Los Angeles, CA 90095; ^cDepartment of Chemistry, University of California, Los Angeles, CA 90095; ^dInstitute of Structural and Chemical Biology, Department of Molecular and Cell Biology, University of Leicester, Leicester LE1 7RH, United Kingdom; and ^eDepartment of Medicine, Washington University School of Medicine, St. Louis, MO 63110

Contributed by Peter Tontonoz, December 2, 2020 (sent for review November 23, 2020; reviewed by Steven A. Kliewer and Hongyuan Yang)

The Aster proteins (encoded by the *Gramd1a-c* genes) contain a ligand-binding fold structurally similar to a START domain and mediate nonvesicular plasma membrane (PM) to endoplasmic reticulum (ER) cholesterol transport. In an effort to develop small molecule modulators of Asters, we identified 20 α -hydroxycholesterol (HC) and U18666A as lead compounds. Unfortunately, both 20 α -HC and U18666A target other sterol homeostatic proteins, limiting their utility. 20 α -HC inhibits sterol regulatory element-binding protein 2 (SREBP2) processing, and U18666A is an inhibitor of the vesicular trafficking protein Niemann–Pick C1 (NPC1). To develop potent and selective Aster inhibitors, we synthesized a series of compounds by modifying 20 α -HC and U18666A. Among these, AI (Aster inhibitor)-1I, which has a longer side chain than 20 α -HC, selectively bound to Aster-C. The crystal structure of Aster-C in complex with AI-1I suggests that sequence and flexibility differences in the loop that gates the binding cavity may account for the ligand specificity for Aster C. We further identified the U18666A analog AI-3d as a potent inhibitor of all three Aster proteins. AI-3d blocks the ability of Asters to bind and transfer cholesterol *in vitro* and in cells. Importantly, AI-3d also inhibits the movement of low-density lipoprotein (LDL) cholesterol to the ER, although AI-3d does not block NPC1. This finding positions the nonvesicular Aster pathway downstream of NPC1-dependent vesicular transport in the movement of LDL cholesterol to the ER. Selective Aster inhibitors represent useful chemical tools to distinguish vesicular and nonvesicular sterol transport mechanisms in mammalian cells.

shown to impair the movement of cholesterol from the PM to the ER (10, 15), suggesting that it may also target as-yet undefined sterol transport pathways.

Blood levels of high-density lipoprotein (HDL) cholesterol are inversely associated with heart disease. However, recent clinical studies have shown that simply raising HDL cholesterol does not protect against cardiovascular disease (16). This suggests that the flux of cholesterol to and from HDL may be more relevant to arterial lipid deposition than static blood levels. The Aster proteins (encoded by the *Gramd1a,b,c* genes) have recently been identified as a mechanism for movement of HDL-derived cholesterol into cells (17). Aster-B is selectively enriched in steroidogenic tissues and its function is critical for the storage of cholesteryl ester (CE) and steroidogenesis in the adrenal cortex (17). Cellular studies have shown that all three Asters facilitate nonvesicular PM-ER sterol trafficking. Asters are anchored to the ER by a single transmembrane helix. Their central domain (termed the ASTER domain) structurally resembles a START domain and binds cholesterol and certain oxysterols. The N-terminal GRAM domain binds phosphatidylserine and mediates Aster recruitment to PM-ER contact sites in response to cholesterol accumulation in the PM. Recent studies have implicated Aster proteins in the regulation of the metabolically active “accessible” cholesterol pool in the plasma membrane (18, 19).

The cell type-selective expression of Asters in metabolic tissues implies that these transporters are likely to play roles in lipid

cholesterol | lipid transport | lipid metabolism

Elevated blood levels of low-density lipoprotein (LDL) are a major risk factor for cardiovascular disease. Mammalian cells take up LDL by receptor-mediated endocytosis and traffic it to the lysosomes where free cholesterol is liberated (1). The Niemann Pick type C proteins 1 and 2 (NPC1, NPC2) are critical for the export of LDL-derived cholesterol from lysosome (2, 3). NPC1 transfers cholesterol to the lysosomal membrane for delivery to other cellular membranes. Mutations in either NPC1 or NPC2 lead to the accumulation of lysosomal lipids—phenotypes associated with Niemann Pick type C disease (4, 5). The pathways that traffic cholesterol to the endoplasmic reticulum (ER) downstream of NPC1 are incompletely characterized, although evidence suggests that cholesterol from lysosomes may move to the plasma membrane (PM) prior to reaching the ER (6–8).

The androstrenolone derivative U18666A has been used as a tool for the study of LDL-derived cholesterol transport. U18666A binds to the sterol-sensing domain (SSD) of NPC1 and, thereby, inhibits the export of cholesterol from lysosomes (9). Furthermore, exogenous cholesterol is unable to suppress the SRBP2 pathway or undergo esterification in the presence of U18666A, indicating that cholesterol movement to ER is disrupted (10, 11). In addition, U18666A inhibits at least three membrane-bound enzymes in sterol synthesis: 2,3-oxidosqualene cyclase, sterol D8–D7 isomerase, and desmosterol reductase (12–14). U18666A has also been

Significance

The Aster proteins are transporters that move cholesterol between the plasma membrane and the ER. Here, we develop and characterize small molecules that selectively inhibit one or more Aster proteins. Importantly, we identify compounds that block Aster-mediated cholesterol transport without interfering with other sterol regulatory proteins, including NPC1 and SREBP2. Cell studies reveal that inhibition of Aster function by small molecules blocks the movement of LDL-derived cholesterol from the plasma membrane to the ER, thus positioning the nonvesicular Aster pathway downstream of the NPC1 vesicular pathway in the movement of LDL-derived cholesterol.

Author contributions: X.X., Y.K., B.R.-A., J.W.R.S., M.E.J., and P.T. designed research; X.X., Y.K., B.R.-A., and K.S. performed research; D.S.O. contributed new reagents/analytic tools; X.X., Y.K., B.R.-A., K.S., J.W.R.S., M.E.J., and P.T. analyzed data; and X.X., Y.K., J.W.R.S., M.E.J., and P.T. wrote the paper.

Reviewers: S.A.K., The University of Texas Southwestern Medical Center; and H.Y., The University of New South Wales.

The authors declare no competing interest.

Published under the PNAS license.

¹X.X., Y.K., and B.R.-A. contributed equally to this work.

²To whom correspondence may be addressed. Email: ptontonoz@mednet.ucla.edu.

This article contains supporting information online at <https://www.pnas.org/lookup/suppl/doi:10.1073/pnas.2024149118/-DCSupplemental>.

Published December 29, 2020.

metabolism in a variety of contexts. Thus, there is a need for chemical tools that selectively target Aster-dependent nonvesicular cholesterol transport. In the current study, we used a combination of synthetic medicinal chemistry, cell biology, and structural biology to identify small molecules that selectively inhibit Asters. Initial screens identified two lead sterol analogs—20 α -HC and U18666A—that bound avidly to all three Aster proteins. To develop selective inhibitors, we prepared a series of compounds by modifying 20 α -HC and U18666A. We identified a potent pan-Aster inhibitor, as well as one that selectively inhibits Aster-C. Functional studies showed that these compounds block the ability of Asters to bind and transfer cholesterol between membranes *in vitro* and antagonize the ability of exogenous cholesterol to suppress SREBP2 processing and be converted to CE in cells. Finally, we show that Aster inhibitors interfere with the movement of LDL cholesterol to the ER, indicating that the Aster pathway functions downstream of NPC1 in the trafficking of LDL-derived cholesterol.

Results

20 α -HC and U18666A Avidly Bind to Asters. The central ASTER domain of the Aster proteins forms a hydrophobic pocket that binds cholesterol and promotes its transfer between membranes (17).

To screen for small molecules that compete with cholesterol for binding this pocket, we performed binding assays using a fluorescent cholesterol derivative, 22-NBD-cholesterol (22-(*N*-(7-nitrobenzo-2-oxa-1,3-diazol-4-yl)amino)-23,24-bisnor-5-cholen-3 β -ol) (17, 20). We purified the ASTER domain of all three Aster proteins (Aster-A_{334–562}, Aster-B_{303–533}, and Aster-C_{296–517}) for use in these assays (SI Appendix, Fig. S1A). Consistent with prior results, binding of 22-NBD-cholesterol to the ASTER domain was inhibited by 25-hydroxycholesterol (25-HC) and cholesterol itself (SI Appendix, Fig. S1B and C) (17).

To identify other compounds that bound to the ASTER domain, we performed a preliminary screen with a variety of oxysterols and steroid-like molecules. Interestingly, the three Asters showed differential binding to various oxysterols (Fig. 1A). 20 α -HC showed high affinity binding to both Aster-B and Aster-C, but more moderate binding to Aster-A. To our surprise, U18666A—a chemical tool widely used to inhibit NPC1 (9)—also bound avidly to Asters (Fig. 1A and B). Our previous crystal structure of the ASTER domain from Aster-A in complex with 25-HC showed there was a glycerol molecule (derived from the crystallization buffer) located adjacent to the 3-OH group of 25-HC (17). Interestingly, the combined space occupied by the

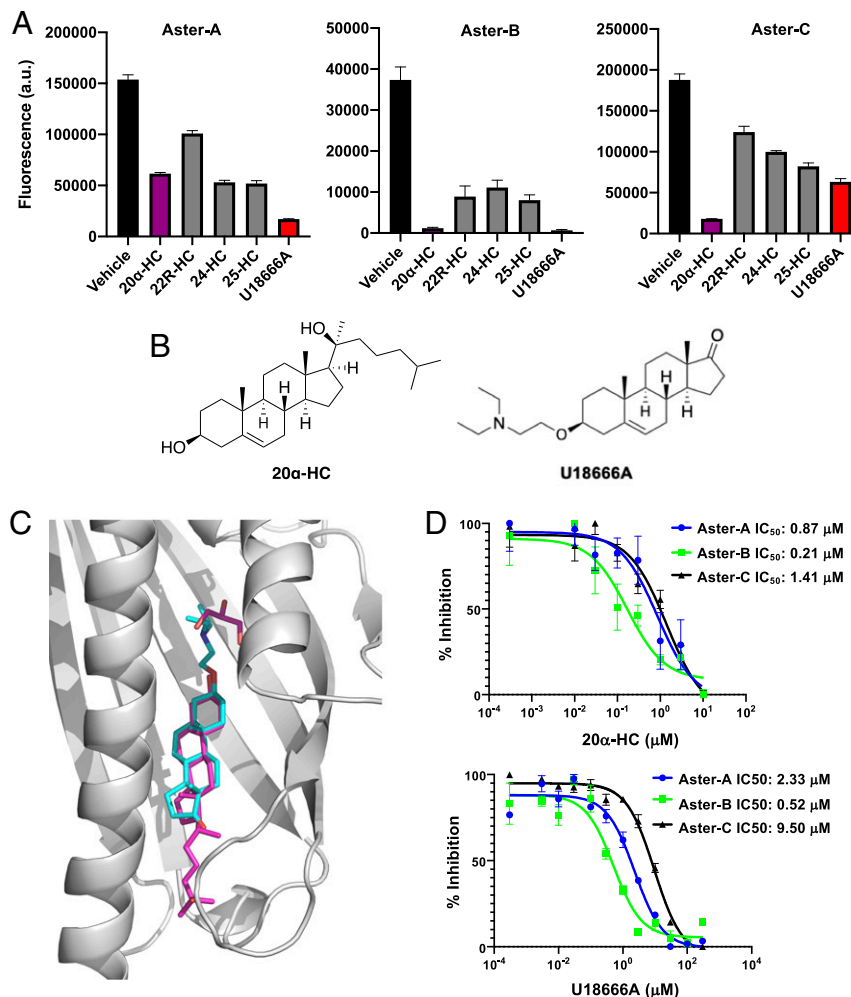


Fig. 1. Identification of 20 α -HC and U18666A as Asters ligands. (A) Competition assay in which purified Aster domains were incubated with 22-NBD-cholesterol in the presence of vehicle, 20 α -HC, 22R-HC, 24-HC, 25-HC, or U18666A competitors (10 μ M). Data bars represent means \pm SD. (B) Structures of 20 α -HC and U18666A. (C) The ligand binding pocket in Aster-A is sufficiently large to accommodate U18666A. The gray cartoon and magenta ligand show the structure of the ASTER domain from Aster-A bound to 25-OH cholesterol and a glycerol molecule from the crystallization buffer. The cyan ligand is U18666A modeled into the extended ligand binding pocket. (D) Half-maximum inhibitory concentration (IC₅₀) values of 20 α -HC and U18666A for Asters. Dose–response curves were determined by nonlinear regression. All data are shown as mean \pm SEM.

glycerol and 25-HC in the pocket is sufficient to accommodate U18666A (modeled in Fig. 1C). Dose–response experiments determined the IC₅₀ values of 20 α -HC for Asters (A: 0.87 μ M, B: 0.21 μ M, C: 1.41 μ M) and of U18666A for Asters (A: 2.33 μ M, B: 0.52 μ M, and C: 9.50 μ M; Fig. 1D). In contrast to its affinity for Asters, U18666A was a poor competitor for binding to StARD1 (*SI Appendix*, Fig. S1D).

U18666A Blocks the Ability of Asters to Transfer Cholesterol between Membranes. To test the hypothesis that U18666A might block nonvesicular sterol transport pathways, we tested the effect of U18666A on the movement of cholesterol by Asters. We performed *in vitro* assays with heavy and light liposomes (17, 21). As expected, the ASTER domain from Aster-A, Aster-B, or Aster-C efficiently facilitated cholesterol transfer (*SI Appendix*, Fig. S1E). Moreover, the addition of U18666A decreased the ability of Asters to transfer cholesterol between liposomes in a dose-dependent manner (Fig. 2A). By contrast, U18666A had minimal effect on StARD1 cholesterol transport capacity, in line with its poor binding to StARD1 (*SI Appendix*, Fig. S1F).

U18666A has been demonstrated to inhibit vesicular cholesterol transport through the lysosomal NPC1/2 pathway and to antagonize the suppression of SREBP2 cleavage by exogenous cholesterol (9). To examine potential NPC1-independent effects of U18666A on sterol transport, we used an NPC1-null (KO) cell line (CHO-M12; *SI Appendix*, Fig. S2A) (22). These cells accumulate lysosomal cholesterol, as revealed by filipin staining (*SI Appendix*, Fig. S2B). U18666A has also been reported to inhibit at least three sterol synthesis enzymes (12–14). To exclude any contribution of endogenous sterol synthesis to SREBP2 regulation in our assays, we treated the cells with simvastatin, an inhibitor of HMGCR (the rate limiting enzyme of cholesterol synthesis). Treatment of CHO-M12 cells cultured under sterol-depleted conditions (lipoprotein-deficient serum and statin treatment) with U18666A did not inhibit SREBP2 processing (*SI Appendix*, Fig. S2C). Thus, U18666A does not share the inhibitory effects of oxysterols such as 25-HC on SREBP2 processing. However, we found that the ability of exogenously added cyclodextrin cholesterol to suppress SREBP2 processing (Fig. 2B), and the expression of SREBP2 target genes (Fig. 2C) was substantially reduced by U18666A treatment of CHO-M12 cells. These findings strongly suggest that U18666A inhibits cholesterol transport to the ER downstream of NPC1. Consistent with this idea, we found that CE formation was reduced in CHO-M12 cells treated with U18666A (Fig. 2D).

To further determine whether the effects of U18666A on SREBP2 processing and CE formation in NPC1 KO cells were due specifically to Aster inhibition, we generated an Aster-A, Aster-B, and Aster-C triple knockdown cell line on the background of the NPC1 KO (M12 ABC-KD) (*SI Appendix*, Fig. S2D). We found that the ability of exogenously added cyclodextrin cholesterol to suppress SREBP2 processing was reduced in M12 ABC-KD cells compared to parent (control) M12 cells and that treatment with U18666A did not cause further inhibition (Fig. 2E and *SI Appendix*, Fig. S2D). We conclude that U18666A blocks the ability of Asters to bind and transfer cholesterol between membranes. Thus, U18666A is an inhibitor of both vesicular (NPC1-dependent) and nonvesicular (Aster-dependent) cholesterol transport pathways.

Design and Synthesis of Asters Ligands. We designed Aster inhibitory compounds by modifying the structure of 20 α -HC and U18666A in different ways (*SI Appendix*, Fig. S3A). Details on compound synthesis and validation are provided in *SI Appendix*, *Supplemental Methods*. Pregnenolone [4] was used as starting material. We introduced various lengths of alkyl side chains from one to eight carbons at C20 to assess the change in binding activity (23). In addition, compounds 2 and 3 were designed and synthesized to include an OH group at C20 to improve solubility and a variety of

aminoalkyl groups on the oxygen at C3 (9, 24, 25). Grignard reagents with a variety of alkyl group were coupled to TBS-protected pregnenolone [5] to give a single (*S*)-stereoisomer intermediate (*SI Appendix*, Fig. S3B) (23). To confirm the structure–activity relationships, 13 different alkyl side chain were employed. After deprotection of the TBS group using TBAF, compounds 1a–1m were obtained. Compounds 2a–2g were synthesized from 1a or 1k via alkylation with 2-bromo-*N,N*-dialkylacetamides (25). The reduction of amide group of compounds 2 using LAH was carried out to yield the compounds 3a–3g from the corresponding amides.

Aster-C Preferentially Binds to 20 α -HC Analogs with Extended Side Chains. We investigated the effect of varying the length of the alkyl side chain at C20 on the ability to bind Aster-A, Aster-B, and Aster-C (Fig. 3A and B). U18666A was used as the reference compound. Compound 1a, which includes a methyl group, was an efficient competitor for NBD-cholesterol binding to Aster-B, but not Aster-A or Aster-C. Compounds 1b and 1c, which include ethyl and propyl side chains, respectively, also showed the same tendency. Compound 1d, which includes a butyl group, showed strong inhibition of binding to Aster-B and moderate inhibition of Aster-C. Compound 1e, which includes a pentyl chain, showed moderate inhibition of Aster-A, and potent inhibition of Aster-B and Aster-C. Interestingly, compounds with a side chain of more than five carbons in length showed relatively poor inhibition of Aster-A and Aster-B. Compound 1f, which includes a six-carbon side chain, was relatively selective for Aster-C inhibition. However, compounds with longer carbon chains (1g and 1h) were less effective inhibitors of Aster-C than compound 1f. Together these results show that the five-carbon alkyl chain of compound 1e is the optimal length for inhibition of sterol binding to Aster-A and Aster-B, while the six-carbon chain of compound 1f is better suited to inhibition of Aster-C.

Competition binding assays were also conducted for compounds 1i–1m, which have isoalkyl side chains similar to cholesterol (Fig. 3C). Compounds 1i and 1j, which include relatively short side chains, were most effective against Aster-B. Compound 1l, which includes the same length with a six-carbon isoheptyl chain, was a strong inhibitor of binding to Aster-C, but not Aster-A or Aster-B (Fig. 3D). We selected compound 1l for further study and determined its IC₅₀ for Aster-C to be 0.85 μ M (Fig. 3E). This represents an improvement of 1.6-fold compared to 20 α -HC and 11.2-fold compared to U18666A.

Structure of the Aster-C Sterol-Binding Domain in Complex with AI-11.

To understand why compound 1l might bind preferentially to Aster C, we crystallized the ASTER domain of Aster C (amino acids 296–517) bound to AI-11 (*SI Appendix*, Table S1). The structure was determined by molecular replacement using our previous structure of the ASTER domain from Aster-A with 25-hydroxycholesterol (Protein Data Bank [PDB] ID code: 6GQF) (17). These two domains have 51% sequence identity. As expected, the two structures are very similar, with a highly curved seven-stranded β -sheet forming a groove to accommodate the AI-11 ligand (Fig. 4A). The electron density clearly defines the position and orientation of the AI-11 ligand (Fig. 4B), which is very similar to the position of the 25-hydroxycholesterol in the ASTER domain from Aster-A (Fig. 4C). This position appears to be determined by inward facing residues on the C-terminal helix of the ASTER domain (Fig. 5A). The key interactions are between the axial methyl group C19 and the sterol ring A with a critical tyrosine residue Y481 (Y524 in Aster-A) and the axial methyl C18 resting closely against serine S477 (G520 in Aster-A).

Interestingly, as was observed for the Aster-A structure bound to 25-hydroxycholesterol, there is additional volume within the sterol-binding pocket of Aster-C adjacent to the C3-OH group of the AI-11 ligand and adjacent to the third sterol ring (*SI Appendix*, Fig. S4). The electron density suggests that this extra space is

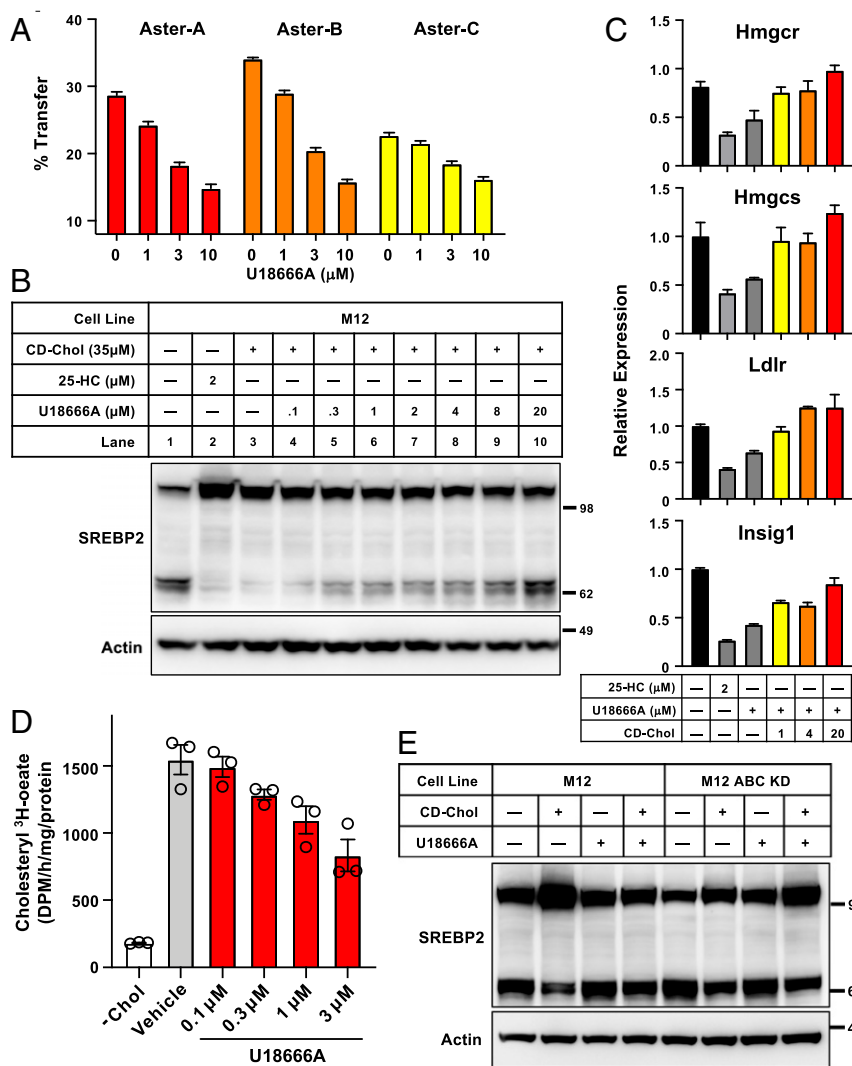


Fig. 2. U18666A blocks the ability of Asters to transfer cholesterol between membranes. (A) Sucrose-loaded heavy PC/dansyl-PE liposomes and light PC/dansyl-PE-cholesterol liposomes were incubated with 6 μM Aster-A_{334–562}, Aster-B_{303–533}, or Aster-C_{296–517} in the presence of vehicle or U18666A for 20 min at 25 °C. Cholesterol transfer to the heavy liposomes was assessed and normalized to dansyl-PE recovery. Values are means ± SD. (B) U18666A inhibits the cleavage of endogenous SREBP2 in the M12 (NPC1 KO) cell line. M12 cells were depleted of sterols by incubating in medium containing 1% lipoprotein-deficient serum (LPDS), simvastatin (5 μM) and mevalonate (10 μM) for 16 h at 37 °C. Cells were then switched to the same medium with vehicle or increasing concentrations of U18666A for 4 h. Cells were then treated with or without 35 μM mβCD-cholesterol/2 μM 25-HC for another 2 h. Immunoblots were performed with anti-SREBP2 antibody (7D4). (C) Expression of SREBP2 pathway genes in the experiment shown in B. Values are means ± SEM. (D) U18666A inhibits cholesteryl [³H]-oleate formation in the NPC1 KO cell line M12. M12 cells were depleted of sterols by incubating in medium containing 1% LPDS, simvastatin (5 μM), and mevalonate (10 μM) for 16 h at 37 °C. Cells were switched to the same medium with vehicle or increasing concentrations of U18666A for 6 h. Cells were labeled for another 4 h with 0.2 mM sodium [³H]-oleate, and content of cholesteryl [³H]-oleate was determined. Each value is the average of triplicate incubations. Values are means ± SD. (E) M12 or M12 Aster-ABC KD cells were depleted of sterols by incubating in medium containing 1% LPDS, simvastatin (5 μM), and mevalonate (10 μM) for 16 h at 37 °C. Cells were switched to the same medium with vehicle or U18666A (10 μM) for 6 h. Cells were then treated with or without 35 μM mβCD-cholesterol for another 2 h. Immunoblots were performed with anti-SREBP2 antibody.

occupied by a glycerol and an ethanol molecule adjacent to the C3-OH, and another ethanol molecule adjacent to the third sterol ring. There are also four molecules of water within the binding pocket. Taken together, these findings indicate that the binding pocket of Aster-C is slightly bigger than that of Aster-A. Analysis with the Pocket-Cavity Search Application (26) showed that the Aster-C cavity measures 465 Å³ and the Aster-A cavity 453 Å³ (SI Appendix, Fig. S4).

We carefully inspected the structure to understand why AI-11 might bind preferentially to Aster-C. A key difference between the Aster proteins is the loop that closes over the sidechain of the ligand distal to the C3-OH. This loop appears relatively

flexible judging by higher B factors and multiple conformations in different structures. The details of how tightly the loop can adapt to a bound ligand is likely to influence the on/off rate for the different ligands and, thus, determine the overall binding affinity and specificity. Fig. 5B highlights the differences in the Aster-A and Aster-C loops and ligand interactions, including a key interaction in Aster-C between T393 and the AI-11 ligand.

Development of U18666A Analogs that Selectively Bind Asters. In order to develop more Aster-selective ligands, we analyzed the binding activities of compounds 2a–2g and 3a–3g, which were prepared from compounds 1a and 1k with *N,N*-dialkylacetamide

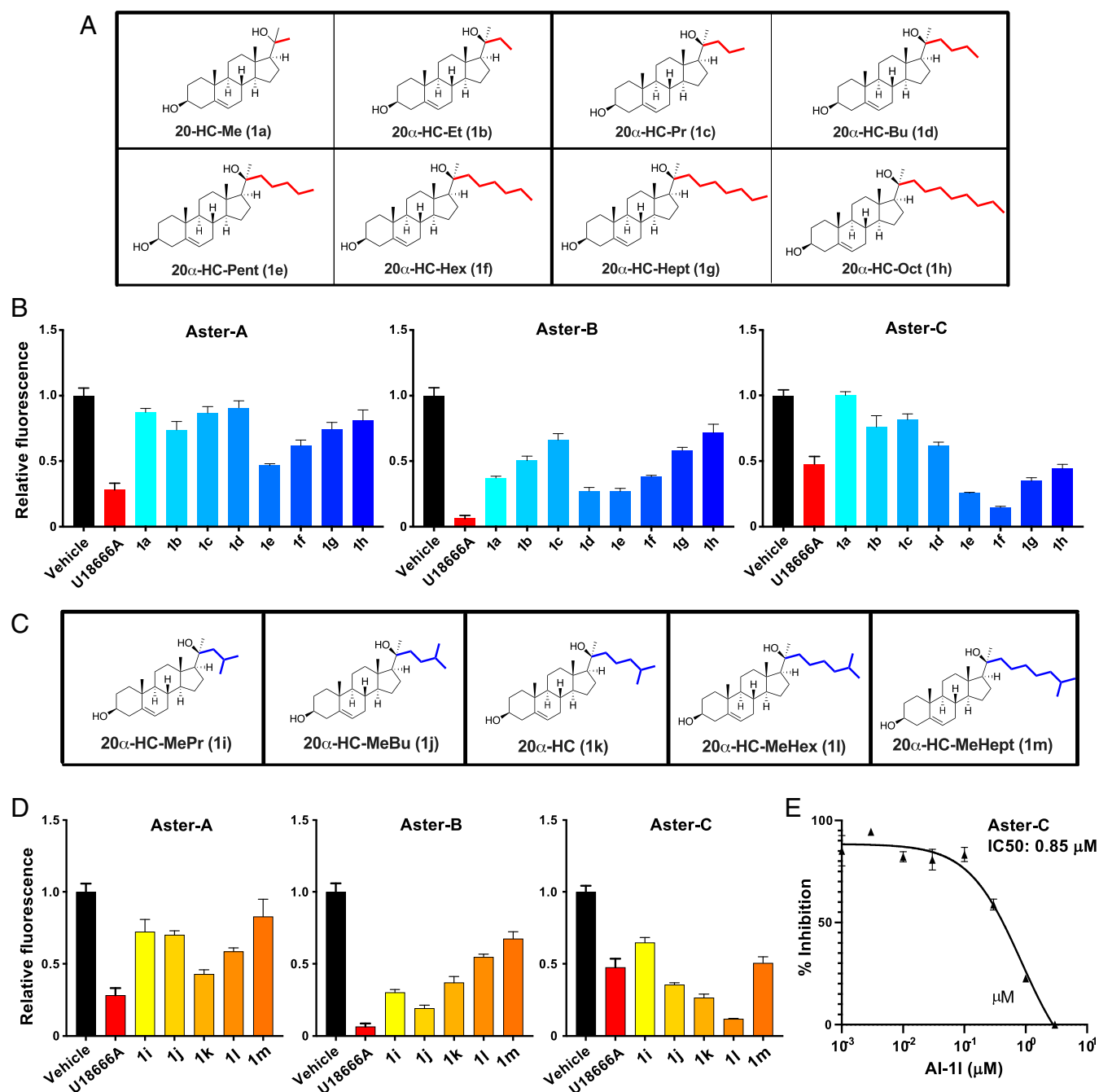


Fig. 3. Aster-C prefers binding to 20 α -HC analogs with hexyl side chains. (A) Structures of 20 α -HC analog Aster inhibitors 1a–1h with linear *n*-alkyl side chains. (B) Purified Aster domains were titrated with 22-NBD-cholesterol in the presence of vehicle, U18666A, and 20 α -HC analogs as indicated (10 μ M). Data bars represent means \pm SD. (C) Structures of 20 α -HC analog Aster inhibitors 1i–1m with branched isoalkyl side chains. (D) Purified Aster domain was titrated with 22-NBD-cholesterol in the presence of vehicle, U18666A, and 20 α -HC analogies 1a–1h as indicated (10 μ M). Data bars represent means \pm SD. (E) IC₅₀ value for 1l binding to Aster-C_{296–517} was measured in the presence of varying concentrations of 1l. Dose–response curve was determined by nonlinear regression. All data are shown as mean \pm SEM.

or *N,N*-dialkylamino ethyl groups, respectively (Fig. 6A). Among the compounds with a dialkylacetamide unit, compounds 2a, 2b, 2c, 2d, 2e, and 2g showed moderate inhibition of Aster-A, Aster-B, and Aster-C binding, whereas compound 2f showed prominent inhibition of all three Asters (Fig. 6B). Among the compounds with dialkylaminoethyl groups, 3a (with a dimethylamino group), 3b (with a diethylamino group), and 3e (with a piperidine group) showed robust inhibition of all three Aster proteins. Compound 3f (with a morpholine group) was a more effective

competitor for binding to Aster-A and Aster-B than to Aster-C. Compounds 3c (with a dipropylamino group) and 3d (with a pyrrolidine group) showed excellent activity against Aster-A, Aster-B, and Aster-C. Compound 3g with diethylaminoethyl group at 3-OH and an isohexyl group at C20 also showed strong inhibition of Aster binding (Fig. 6B). We determined IC₅₀ values for AI-3a and AI-3d against Aster-A, Aster-B, and Aster-C (AI-3a, A: 0.74 μ M, B: 0.94 μ M, C: 2.86 μ M and AI-3d, A: 0.11 μ M, B: 0.06 μ M, C: 0.71 μ M) (Fig. 6 C and D). A recent study identified

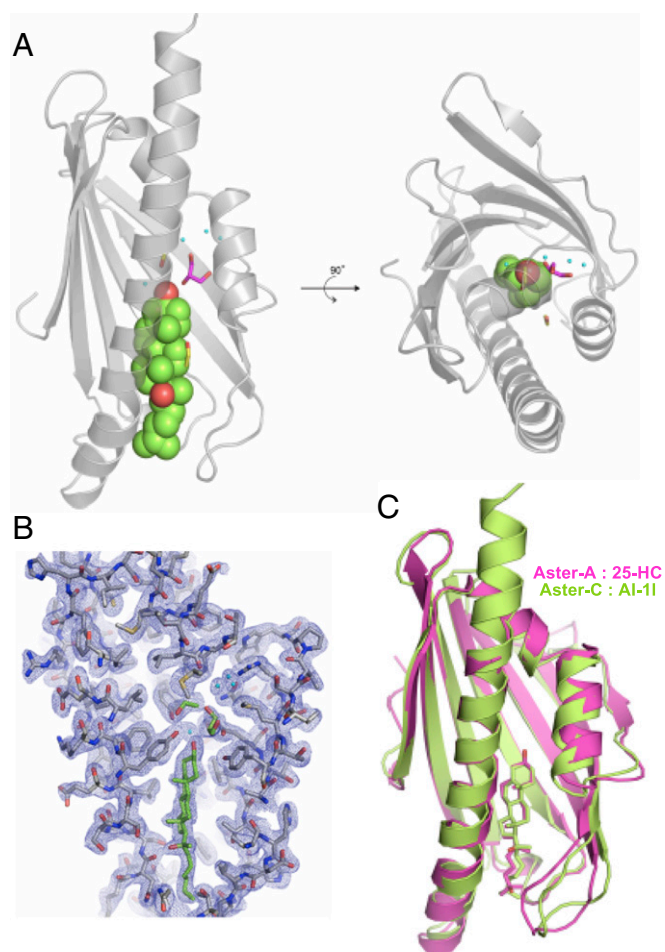


Fig. 4. The structure of AsterC:AI-11 and comparison with AsterA:25-HC. (A) The AI-11 ligand (green) fits snugly in a pocket created between the highly curved beta-sheet and carboxyl-terminal helix. (B) 2Fo-Fc electron density map of AI-11 (green) bound to Aster-C. The cavity also accommodates glycerol, ethanol, and water molecules. The C20-OH makes a hydrogen bond with the backbone carbonyl of Asn473 in the long C-terminal helix (left in figure). (C) Superposition of the structure of Aster-C:AI-11 (green) with Aster-A:25-HC (magenta). The architecture of the domains is very similar, although the C-terminal helix is longer in Aster-C (top left), and the loop conformation closing the ligand pocket is distinct (bottom right).

autogramin-2 as an inhibitor of Aster-A (27). We confirmed this and further showed that AI-3d is a more potent inhibitor than autogramin-2 (*SI Appendix, Fig. S5 A–C*). Autogramin-2 is a comparatively poor inhibitor of Aster-B and Aster-C.

Biological Activity of Aster Inhibitors. Next, we focused on the biological activity of our Aster inhibitors. We first assessed the activity of the three 20 α -HC analogs that showed selectivity for Aster-C (AI-1e, AI-1f, and AI-1l). We performed filipin staining for free cholesterol on WT CHO-K1 cells cultured in cholesterol-containing media. In contrast to U18666A, AI-1e, AI-1f, and AI-1l did not cause lysosomal cholesterol accumulation (*SI Appendix, Fig. S6A*). We next assessed the ability of the AI-1e, 1f, and 1l to affect SREBP2 processing. Each of these 20 α -HC analogs retained the ability of 20 α -HC to inhibit SREBP2 processing (*SI Appendix, Fig. S6B*). Thus, although 1e, 1f, and 1l do not target NPC1, they still interact with the SREBP pathway in addition to blocking Asters.

We next focused on the series of Aster inhibitors adapted from U18666A (AI-3a, AI-3b, AI-3c, AI-3d, AI-3e, AI-3f, and AI-3g). Again, we performed filipin staining for free cholesterol on WT

CHO-K1 cells to assess NPC1 inhibition. Treatment with AI-3g, which contains structural elements of both U18666A and 20 α -HC, led to substantial filipin staining, indicating that it retained the ability to interact with NPC1 (*SI Appendix, Fig. S6C*). By contrast, AI-3a and AI-3d did not cause lysosomal cholesterol accumulation, even at a concentration of 10 μ M (Fig. 7A). We also assessed effects on SREBP2 processing. Compounds AI-3a, AI-3d, and AI-3g did not inhibit SREBP2 processing (*SI Appendix, Fig. S6D* and Fig. 7B). Based on these data, AI-3d was selected for further experiments.

AI-3d Blocks Cholesterol Transfer by Asters. Using our liposome transfer assay, we determined that AI-3d efficiently inhibited Aster-mediated cholesterol transfer (Fig. 7C). We further found that addition of cyclodextrin-cholesterol suppressed SREBP2 processing in control CHO K1 cells and that treatment with AI-3d abolished the ability of exogenous cholesterol to suppress SREBP2 processing (Fig. 7D and *SI Appendix, Fig. S6E*). Exogenous cholesterol was unable to suppress SREBP2 processing in CHO ABC-KD cells, and treatment with AI-3d did not further inhibit SREBP2 processing. In line with its effects on SREBP2 processing, AI-3d also regulated CE formation in cells. Consistently, the rate of cholesterol incorporated into CE was markedly lower in CHO ABC-KD cells compared to CHO K1 cells (Fig. 7E). CE formation was strongly reduced by treatment with AI-3d in both CHO K1 cells and CHO ABC-KD cells. Prior studies have pioneered the use of the modified cytolysin ALO-D4 to detect the accessible PM cholesterol pool (7). In line with our evidence of less cholesterol reaching the ER in the presence of AI-3d analysis of ALO-D4, staining by confocal microscopy revealed increased accessible PM cholesterol in cells treated with AI-3d (Fig. 7F).

LDL is internalized into cells by receptor-mediated endocytosis, and its component cholesterol is thereby delivered to lysosomes. NPC1 is required for cholesterol to exit the lysosome, but the route and mechanism of cholesterol movement downstream of NPC1 remains to be clarified. We found that AI-3d treatment of CHO cells interfered with the ability of LDL to suppress SREBP2 cleavage (Fig. 7G). This finding strongly suggests that Aster-dependent nonvesicular transport pathways are involved in the movement of LDL-cholesterol from PM to the ER after it leaves the lysosome. Collectively, our data identify AI-3d as an Aster-selective inhibitor that blocks nonvesicular PM to ER cholesterol transfer.

Discussion

The three Aster family members are expressed in a tissue-specific manner. Aster-B, which is highly expressed in steroidogenic tissues, is to date the only putative mammalian PM–ER cholesterol transporter to show a loss-of-function phenotype in vivo. Mice lacking Aster-B are defective in the transport of HDL-derived cholesterol from SR-BI to the ER in the adrenal cortex (17). The physiological functions of the other two Aster family members remain to be established. The observations that Aster-A and Aster-C are also recruited to cholesterol-enriched plasma membranes and mediate PM to ER cholesterol transport in cultured cells strongly suggest that they are involved in the maintenance of sterol homeostasis in one or more tissues in vivo. Here, we report the development of chemical tools selectively targeting Aster proteins that will aid in the experimental dissection of vesicular and nonvesicular sterol transport pathways.

Our early screening results revealed two lead molecules, 20 α -HC and U18666A, that bound avidly to Aster proteins. Interestingly, a previous study used a derivative of U18666A (U-X; which contains a benzophenone and an alkyne group at the 3-hydroxyl of U18666A) to identify binding proteins (9). These studies showed that NPC1 is a major target of U18666A. U18666A binds to the sterol-sensing domain of NPC1 and blocks the movement of cholesterol out of lysosomes. Here, we showed that the Aster pathway

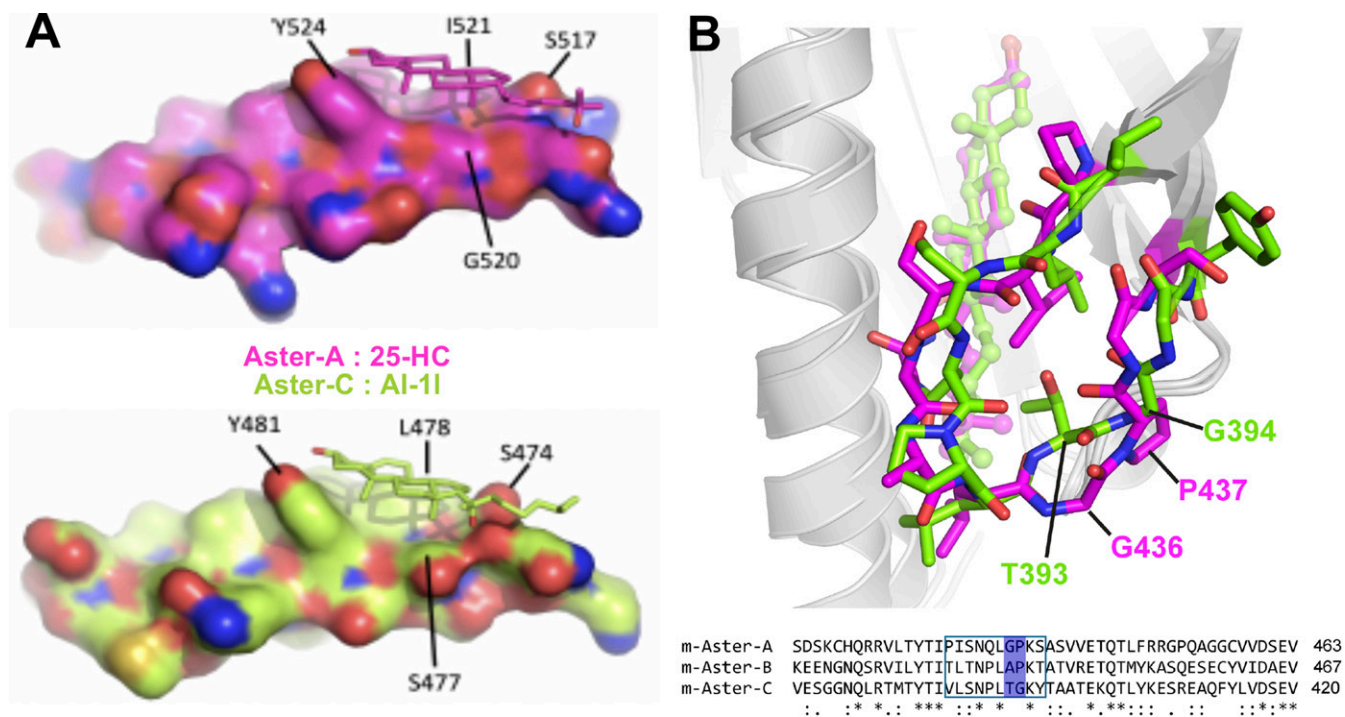


Fig. 5. Basis for selective ligand binding to Aster-A and Aster-C. (A) View of the AI-11 and 25-HC ligands (sticks) interacting with the C-terminal helices of Aster-C and Aster-A, respectively (surface). The position of the ligand in both structures is determined by conserved nonpolar interactions between the sterol ring A and axial C19 methyl with a critical inward facing tyrosine. (B) Details of the loop differences between Aster-A (magenta) and Aster-C (green). A critical proline residue (P437) in Aster-A (conserved in Aster-B) determines the path of the loop. In Aster-C, a glycine (G394) at the same position allows Thr393 to engage with the longer sidechain of the AI-11 ligand.

is also a functional target of U18666A. Based on comparison of the crystal structure of Aster-A in complex with 25-HC and glycerol (17), there is sufficient space in the Aster pocket to accommodate U18666A. However, this space appears too narrow to accommodate U-X, which contains a much bigger benzophenone and an alkyne group at the sterol 3-hydroxyl. Furthermore, the alkynyl group of compound U-X would be expected to be deeply buried in the Aster binding pocket, limiting its accessibility for click chemistry modification. This likely explains why Lu et al. did not identify Asters as binding partners of U18666A (9). Given our demonstration that U18666A blocks the ability of Asters to transport cholesterol in vitro and in cells, caution is warranted when interpreting the biological effects of this chemical tool. It is now clear that U18666A inhibits both vesicular (NPC1-dependent) and non-vesicular pathways (Aster-dependent), and this information may impact prior conclusions drawn using U18666A.

Our studies with 20α -HC analogs revealed that Aster-C preferentially binds to longer side chain analogs. An analog with a six-carbon chain (AI-11) showed optimal preference for Aster-C over Aster-A and Aster-B. We provided molecular insight into this selectivity by solving the crystal structure of Aster-C in complex with AI-11. We compared this structure with that of Aster-A bound to 25-OH cholesterol, where the side chain is one carbon shorter (like that of 20α -HC). This comparison suggests that differences in the amino acids and conformation of the flexible loop which closes over the ligand pocket will likely account for the different ligand specificities. Cell culture studies with our 20α -HC analogs showed that although these compounds did not inhibit NPC1, they did inhibit SREBP2 processing similar to a number of other oxysterols. This interaction may limit the experimental contexts in which AI-11 may be useful as an Aster-C-selective inhibitor.

In an effort to develop more selective Aster inhibitors, we synthesized and profiled a series of U18666A analogs. We identified a

particularly potent analog (AI-3d) that avidly bound all three Asters. AI-3d potentially impairs the ability of Asters to transfer cholesterol between liposomes in vitro. Furthermore, AI-3d blocks the ability of exogenous cholesterol to suppress SREBP2 processing and stimulate CE formation in cells, and these effects are dependent on Aster expression. Our results also shed light on the mechanism by which LDL-derived cholesterol is trafficked to the ER downstream of NPC1. Prior studies have suggested that cholesterol moves first from the lysosome to the PM and then to the ER (6–8). Interestingly, Trinh et al. have recently shown that phosphatidyl serine in the PM is required for LDL cholesterol movement to the ER (28). Since the GRAM domain of Aster proteins binds PS and is responsible for their cholesterol-dependent recruitment to the PM, this finding is consistent with a potential role for Aster proteins downstream of NPC1. Our finding that AI-3d blocks the suppression of the ER SREBP2 pathway by LDL fits well with this model and implicates Aster-mediated nonvesicular transport in the final step of LDL-cholesterol delivery to the ER. We expect that AI-3d will be a useful chemical tool to distinguish vesicular and nonvesicular sterol transport mechanisms in mammalian cells.

Methods

Cell Culture. CHO-K1 cells were obtained from the American Type Culture Collection. M12 NPC1 mutant cells were from Daniel S. Ory (Washington University in St. Louis). All cells were maintained in a 1:1 mixture of F-12K medium and Dulbecco's Modified Eagle's media. The media also contained 100 units/mL penicillin and 100 mg/mL streptomycin and 5% fetal bovine serum. The same media containing 1% lipoprotein-deficient serum was used for low cholesterol conditions.

Protein Expression and Binding Assays. For crystallization studies, sequence encoding mouse Aster-C (296–517) was cloned into pGEX2T (GE Healthcare) with a TEV protease site. Aster-C was expressed in *Escherichia coli* Rosetta (DE3) (Novagen) by growing the transformed Rosetta (DE3) at 37 °C in 2xTY until absorbance at 600 nm was 0.6, then inducing with 40 μ M Isopropyl- β -D-thiogalactopyranoside

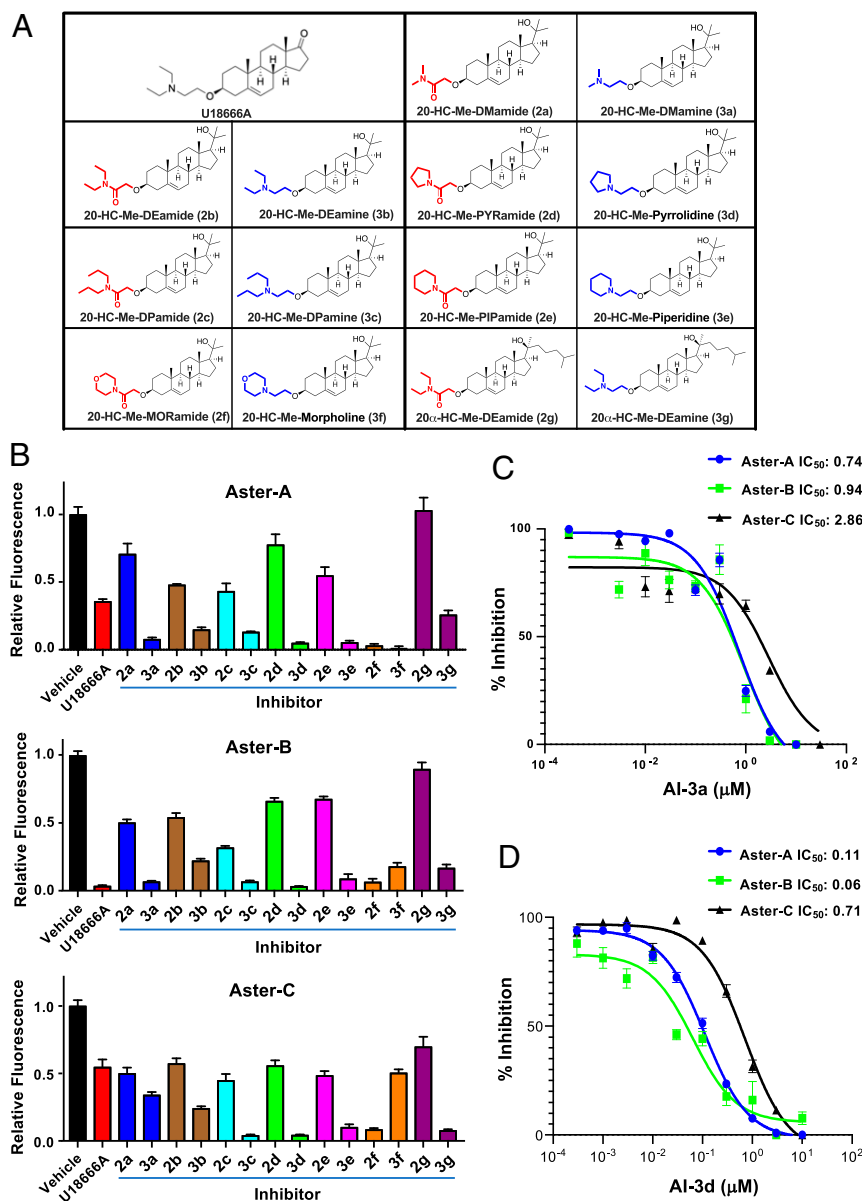


Fig. 6. Characterization of U18666A analog Aster inhibitors. (A) Structures of U18666A analogs. (B) Purified Aster domains (Aster-A_{334–562}, Aster-B_{303–533}, Aster-C_{296–517}) were titrated with 22-NBD-cholesterol in the presence of vehicle, U18666A, and various U18666A analog competitors (10 μ M). Results values are means \pm SD. (C and D). The binding affinity of compounds 3a and 3d to Aster-A_{334–562}, Aster-B_{303–533}, and Aster-C_{296–517} was measured in the presence of varying concentrations of each compound. Dose–response curves for half-maximum inhibitory concentration (IC_{50}) values were determined by nonlinear regression. All data are shown as mean \pm SEM.

(IPTG) and growth overnight at 20 °C. Protein was purified as described previously (17). After the purification excess AI-11 was added (molar ratio 1:5, protein: ligand), the complex purified on a Superdex S-75 column in 50 mM Tris/Cl pH 7.5, 100 mM NaCl and 0.5 mM TCEP. The peak fractions were concentrated to 7.5 mg/mL and used for crystallization. For binding and transfer studies, Aster domains, N-terminal GST Aster-A_{334–562}, Aster-B_{303–533}, Aster-C_{296–517} expression constructs were transformed in Rosetta 2 (DE3) cells (Novagen). Precultures were diluted into large-scale expression cultures and grown at 37 °C to an A_{600} of 0.6–0.8, then induced with 0.5 mM IPTG at 18 °C. Protein was then purified as described previously (17). Fluorescent sterol binding assays were carried out as described (17). Half-maximum inhibitory concentration (IC_{50}) was determined by nonlinear regression analysis of dose–response curves.

Crystallization and X-Ray Structure Determination. Crystals of the Aster-C (296–517) in complex with AI-11 ligand were obtained using sitting drop vapor

diffusion at room temperature as described (17). Crystals were grown using 0.1 M SPG buffer pH 4 (succinic acid, sodium dihydrogen phosphate, and glycine, molar ratio 2:7:7), and 25% polyethylene glycol 1500 (condition A1 PACT, Molecular Dimensions). Data were collected to 2.1 Å on the I24 beamline at Diamond Light Source, UK. Data were processed using XDS (within Xia2) and Pointless/Aimless (within CCP4) (29–32). The structure was solved using molecular replacement using Phaser (within CCP4) and the ASTER domain of Aster-A (PDB ID code 6GQF) (17) as a model (33). Model fitting and refinement were performed using Coot, Refmac (within CCP4), PDB-REDO, and Phenix (34–37). The structure has been submitted to the PDB database, PDB ID code 7AZN.

Gene Expression Analysis. Total RNA was isolated using TRIzol reagent (Invitrogen) and reverse transcribed with iScript (Biorad) as described previously (17). cDNA was quantified by real-time PCR using an ABI 7900. Each gene was analyzed in duplicate and normalized to actin.

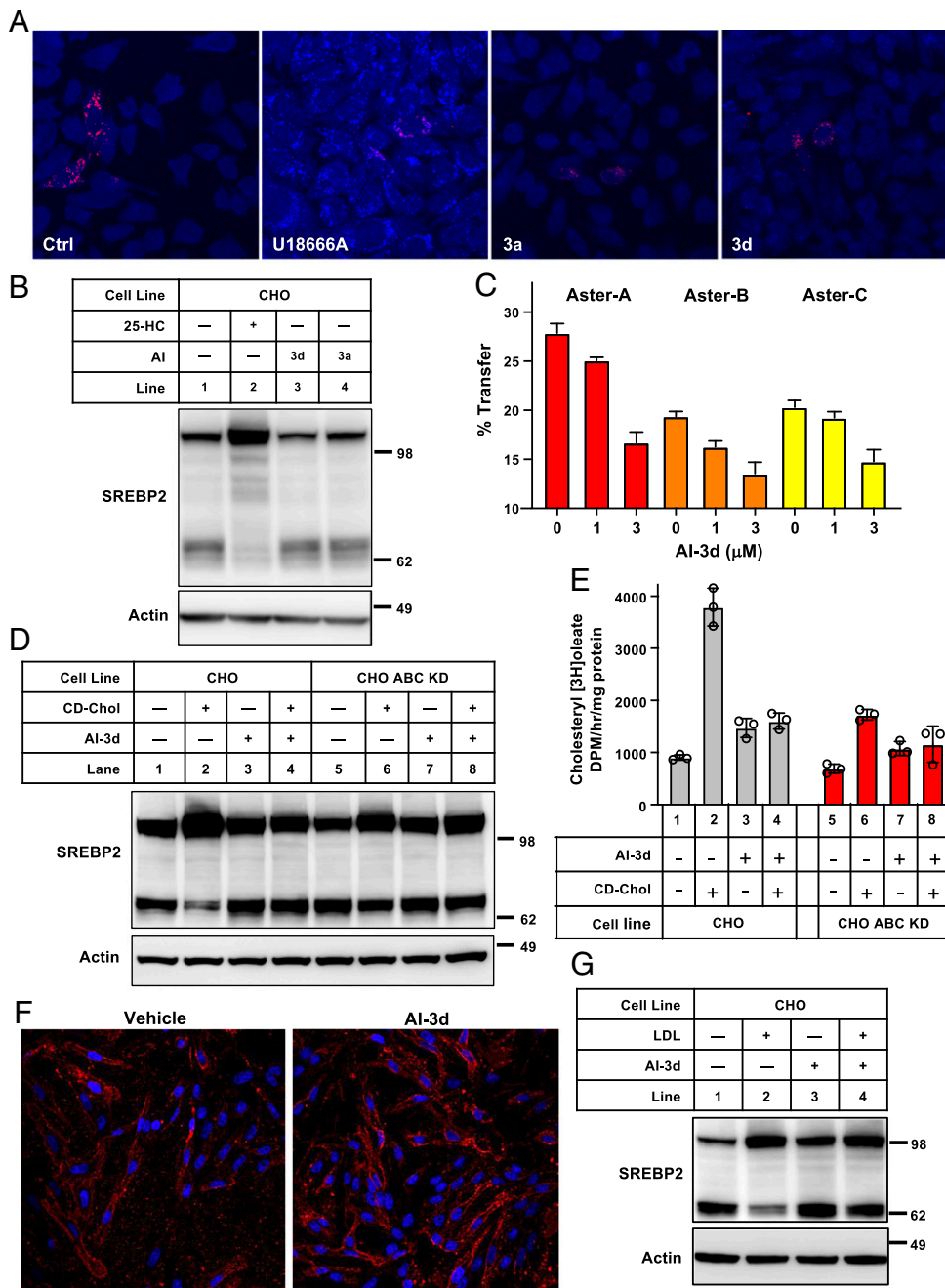


Fig. 7. AI-3d blocks cholesterol transfer by Asters. (A) CHO-K1 cells were incubated in medium A containing 5% FBS and indicated compounds (10 μ M) or vehicle for 6 h at 37 $^{\circ}$ C. Cholesterol and lysosome maker LAMP1 were visualized by filipin staining (pseudo colored blue) and transfected Lamp1-RFP protein (pseudo colored red), respectively. (B) AI-3a and AI-3d do not inhibit the cleavage of endogenous SREBP2. CHO-K1 cells were depleted of sterols by incubating in medium A containing 1% LPDS, simvastatin (5 μ M), and mevalonate (10 μ M) for 16 h at 37 $^{\circ}$ C. Cells were then treated as described in Fig. 2B. After incubation with AI-3a and AI-3d (3 μ M) for 2 h, cells were harvested and immunoblots performed. (C) Sucrose-loaded heavy PC/dansyl-PE liposomes and light PC/dansyl-PE-cholesterol liposomes were incubated with 6 μ M Aster-A₃₃₄₋₅₆₂, Aster-B₃₀₃₋₅₃₃, and Aster-C₂₉₆₋₅₁₇ in the presence of vehicle or Aster inhibitor for 20 min at 25 $^{\circ}$ C. Cholesterol transfer to the heavy liposomes was assessed and normalized to dansyl-PE recovery. Values are means \pm SD. (D) AI-3d inhibits the ability of Asters to transfer exogenous cholesterol to suppress SREBP2 processing. CHO-K1 WT or ABC KD cells were depleted of sterols by incubating in medium A containing 1% LPDS, simvastatin (5 μ M), and mevalonate (10 μ M) for 16 h at 37 $^{\circ}$ C. Cells were switched to the same medium with vehicle or AI-3d (3 μ M) for 6 h. Cells were then treated with same medium with or without 35 μ M m β CD-cholesterol for another 2 h. Immunoblots were performed with anti-SREBP2. (E) AI-3d inhibits cholesteryl [3 H]-oleate formation by blocking Asters. CHO-K1 WT or ABC KD cells were depleted of sterols by incubating in medium containing 1% LPDS, simvastatin (5 μ M), and mevalonate (10 μ M) for 16 h at 37 $^{\circ}$ C. Cells were switched to the same medium with vehicle or AI-3d (3 μ M) for 6 h. Cells were labeled for another 4 h with 0.2 mM sodium [3 H]-oleate. The cells were then harvested for measurement of cholesteryl [3 H]-oleate. Each value is the average of triplicate incubations. Values are means \pm SD. (F) AI-3d inhibits the ability of Asters to transfer cholesterol from the PM. CHO-K1 WT cells were depleted of sterols by incubating in medium containing 1% LPDS, simvastatin (5 μ M), and mevalonate (10 μ M) for 16 h at 37 $^{\circ}$ C. Cells were switched to the same medium with vehicle or AI-3d (3 μ M) for 6 h. Cells were then treated with same medium with or without 35 μ M m β CD-cholesterol for another 1 h. Cells were fixed and stained with ALO-D4. (G) AI-3d interferes with the movement of LDL-derived cholesterol to the ER. CHO-K1 WT cells were depleted of sterols by incubating in medium containing 1% LPDS, simvastatin (5 μ M), and mevalonate (10 μ M) for 16 h at 37 $^{\circ}$ C. Cells were switched to the same medium with vehicle or AI-3d (3 μ M) for 6 h. Cells were then treated with same medium with or without m β CD-cholesterol for another 2 h. Immunoblots were performed with anti-SREBP2.

Chemical Synthesis. Detailed procedures for synthesis and verification of the compounds used in this study are provided in *SI Appendix*. All reactions were conducted under dry argon gas unless otherwise indicated. Commercially available reagents were purchased from Sigma-Aldrich, Oakwood, and AmBeed and used without further purification. Solvents and gases were dried according to standard procedures. Organic solvents were evaporated under reduced pressure using a rotary evaporator. Analytical thin layer chromatography (TLC) was performed using aluminum sheets precoated with silica gel. TLC sheets were visualized by exposure to ultraviolet light and then were visualized with a KMnO₄ or ninhydrin staining solution followed by heating with a heat gun. Flash column chromatography was performed using SilicaFlash P60 (60 Å, 40–63 μm) silica gel with the indicated solvents and compressed air. ¹H and ¹³C NMR spectra were recorded on Bruker 400 and 100 MHz NMR spectrometers. ¹H NMR spectra are represented as follows: chemical shift, multiplicity (s = singlet, brs = broad singlet, d = doublet,

t = triplet, q = quartet, m = multiplet), integration, and coupling constant (*J*) in Hertz (Hz). High-resolution mass spectrometry was performed on a Waters LCT Premier mass spectrometer using an ESI source.

Data Availability. X-ray data have been deposited in the Protein Data Bank (ID code 7AZN).

ACKNOWLEDGMENTS. We thank Jaspreet Sandhu and John P. Kennelly for discussions; Jason Kim, Cuiwen He, Alessandra Ferrari, and Wenxin Song for technical assistance; and Louise Fairall for assistance with X-ray data collection and advice during the refinement. X.X. was supported by American Heart Association Postdoctoral Fellowship 18POST34030388. This work was also supported by NIH Grant HL146358 and Fondation Leducq Grant 19CVD04. Confocal microscopy was performed at the California NanoSystems Institute Advanced Light Microscopy/Spectroscopy Facility.

1. M. S. Brown, J. L. Goldstein, A receptor-mediated pathway for cholesterol homeostasis. *Science* **232**, 34–47 (1986).
2. R. E. Infante *et al.*, Purified NPC1 protein. I. Binding of cholesterol and oxysterols to a 1278-amino acid membrane protein. *J. Biol. Chem.* **283**, 1052–1063 (2008).
3. S. G. Pfisterer, J. Peränen, E. Ikonen, LDL-cholesterol transport to the endoplasmic reticulum: Current concepts. *Curr. Opin. Lipidol.* **27**, 282–287 (2016).
4. D. B. Iaea, F. R. Maxfield, Cholesterol trafficking and distribution. *Essays Biochem.* **57**, 43–55 (2015).
5. M. N. Trinh *et al.*, Triazoles inhibit cholesterol export from lysosomes by binding to NPC1. *Proc. Natl. Acad. Sci. U.S.A.* **114**, 89–94 (2017).
6. H. Wang *et al.*, ORP2 delivers cholesterol to the plasma membrane in exchange for phosphatidylinositol 4, 5-bisphosphate (PI(4,5)P₂). *Mol. Cell* **73**, 458–473.e7 (2019).
7. A. Das, M. S. Brown, D. D. Anderson, J. L. Goldstein, A. Radhakrishnan, Three pools of plasma membrane cholesterol and their relation to cholesterol homeostasis. *eLife* **3**, e02882 (2014).
8. I. Tabas, W. J. Rosoff, G. C. Boykow, Acyl coenzyme A:cholesterol acyl transferase in macrophages utilizes a cellular pool of cholesterol oxidase-accessible cholesterol as substrate. *J. Biol. Chem.* **263**, 1266–1272 (1988).
9. F. Lu *et al.*, Identification of NPC1 as the target of U18666A, an inhibitor of lysosomal cholesterol export and Ebola infection. *eLife* **4**, e12177 (2015).
10. R. J. Cenedella, Cholesterol synthesis inhibitor U18666A and the role of sterol metabolism and trafficking in numerous pathophysiological processes. *Lipids* **44**, 477–487 (2009).
11. L. Liscum, J. R. Faust, The intracellular transport of low density lipoprotein-derived cholesterol is inhibited in Chinese hamster ovary cells cultured with 3-beta-[2-(diethylamino)ethoxy]androst-5-en-17-one. *J. Biol. Chem.* **264**, 11796–11806 (1989).
12. S. H. Bae, Y. K. Paik, Cholesterol biosynthesis from lanosterol: Development of a novel assay method and characterization of rat liver microsomal lanosterol delta 24-reductase. *Biochem. J.* **326**, 609–616 (1997).
13. A. Duriatti *et al.*, In vitro inhibition of animal and higher plants 2,3-oxidosqualene-sterol cyclases by 2-aza-2,3-dihydrosqualene and derivatives, and by other ammonium-containing molecules. *Biochem. Pharmacol.* **34**, 2765–2777 (1985).
14. F. F. Moebius *et al.*, Pharmacological analysis of sterol delta8-delta7 isomerase proteins with [3H]ifenprodil. *Mol. Pharmacol.* **54**, 591–598 (1998).
15. K. W. Underwood, N. L. Jacobs, A. Howley, L. Liscum, Evidence for a cholesterol transport pathway from lysosomes to endoplasmic reticulum that is independent of the plasma membrane. *J. Biol. Chem.* **273**, 4266–4274 (1998).
16. D. J. Rader, A. R. Tall, The not-so-simple HDL story: Is it time to revise the HDL cholesterol hypothesis? *Nat. Med.* **18**, 1344–1346 (2012).
17. J. Sandhu *et al.*, Aster proteins facilitate nonvesicular plasma membrane to ER cholesterol transport in mammalian cells. *Cell* **175**, 514–529.e20 (2018).
18. A. Ferrari *et al.*, Aster proteins regulate the accessible cholesterol pool in the plasma membrane. *Mol. Cell. Biol.* **40**, e00255-20 (2020).
19. T. Naito *et al.*, Movement of accessible plasma membrane cholesterol by the GRAMD1 lipid transfer protein complex. *eLife* **8**, e51401 (2019).
20. W. Wei *et al.*, Ligand activation of ERRα by cholesterol mediates statin and bisphosphonate effects. *Cell Metab.* **23**, 479–491 (2016).
21. J. Chung *et al.*, INTRACELLULAR TRANSPORT. PI4P/phosphatidylserine countertransport at ORP5- and ORP8-mediated ER-plasma membrane contacts. *Science* **349**, 428–432 (2015).
22. S. Jinn *et al.*, snoRNA U17 regulates cellular cholesterol trafficking. *Cell Metab.* **21**, 855–867 (2015).
23. D. Nedelcu, J. Liu, Y. Xu, C. Jao, A. Salic, Oxysterol binding to the extracellular domain of Smoothed in Hedgehog signaling. *Nat. Chem. Biol.* **9**, 557–564 (2013).
24. K. Ohgane, F. Karaki, K. Dodo, Y. Hashimoto, Discovery of oxysterol-derived pharmacological chaperones for NPC1: Implication for the existence of second sterol-binding site. *Chem. Biol.* **20**, 391–402 (2013).
25. K. Ohgane, F. Karaki, T. Noguchi-Yachide, K. Dodo, Y. Hashimoto, Structure-activity relationships of oxysterol-derived pharmacological chaperones for Niemann-Pick type C1 protein. *Bioorg. Med. Chem. Lett.* **24**, 3480–3485 (2014).
26. J. Yu, Y. Zhou, I. Tanaka, M. Yao, Roll: A new algorithm for the detection of protein pockets and cavities with a rolling probe sphere. *Bioinformatics* **26**, 46–52 (2010).
27. L. Laraia *et al.*, The cholesterol transfer protein GRAMD1A regulates autophagosomal biogenesis. *Nat. Chem. Biol.* **15**, 710–720 (2019).
28. M. N. Trinh *et al.*, Last step in the path of LDL cholesterol from lysosome to plasma membrane to ER is governed by phosphatidylserine. *Proc. Natl. Acad. Sci. U.S.A.* **117**, 18521–18529 (2020).
29. W. Kabsch, XDS. *Acta Crystallogr. D Biol. Crystallogr.* **66**, 125–132 (2010).
30. G. Winter, xia2: An expert system for macromolecular crystallography data reduction. *J. Appl. Cryst.* **43**, 186–190 (2010).
31. P. R. Evans, G. N. Murshudov, How good are my data and what is the resolution? *Acta Crystallogr. D Biol. Crystallogr.* **69**, 1204–1214 (2013).
32. M. D. Winn *et al.*, Overview of the CCP4 suite and current developments. *Acta Crystallogr. D Biol. Crystallogr.* **67**, 235–242 (2011).
33. A. J. McCoy *et al.*, Ab initio solution of macromolecular crystal structures without direct methods. *Proc. Natl. Acad. Sci. U.S.A.* **114**, 3637–3641 (2017).
34. P. Emsley, B. Lohkamp, W. G. Scott, K. Cowtan, Features and development of Coot. *Acta Crystallogr. D Biol. Crystallogr.* **66**, 486–501 (2010).
35. G. N. Murshudov *et al.*, REFMAC5 for the refinement of macromolecular crystal structures. *Acta Crystallogr. D Biol. Crystallogr.* **67**, 355–367 (2011).
36. R. P. Joosten, F. Long, G. N. Murshudov, A. Perrakis, The PDB_REDO server for macromolecular structure model optimization. *IUCrJ* **1**, 213–220 (2014).
37. D. Liebschner *et al.*, Macromolecular structure determination using X-rays, neutrons and electrons: Recent developments in Phenix. *Acta Crystallogr. D Struct. Biol.* **75**, 861–877 (2019).